Origin of deactivation of aqueous Na-CO2 battery and mitigation for long-duration energy storage

Ruhul Amin[*,1], Marm Dixit[1], Mengya Li[1], Rachid Essehli[1], Sabine Neumayer[2], Yaocai Bai[1], Anuj Bisht[1], Yang Guang[3], and Ilias Belharouak*[*,1]*

Electrification and Energy Infrastructures Division, Oak Ridge National Laboratory, Oak Ridge, TN, 37830, USA

Center for Nanophase Materials Sciences, Oak Ridge National Laboratory, Oak Ridge, TN, 37830, USA

Chemical Sciences Division, Oak Ridge National Laboratory, Oak Ridge, TN, 37830, USA

*Corresponding Author: aminr@ornl.gov; belharouaki@ornl.gov

Keywords: long duration energy storage, catalyst, deactivation, atomic force microscopy, sodium, carbon dioxide

This manuscript has been authored in part by UT-Battelle, LLC, under contract DE-AC05-00OR22725 with the US Department of Energy (DOE). The publisher, by accepting the article for publication, acknowledges that the US government retains a nonexclusive, paid-up, irrevocable, worldwide license to publish or reproduce the published form of this manuscript, or allow others to do so, for US government purposes. DOE will provide public access to these results of federally sponsored research in accordance with the DOE Public Access Plan (https://www.energy.gov/doe-public-access-plan)

Abstract

The development of long-duration energy storage technology is crucial to facilitate the efficient utilization of renewable energy sources while mitigating carbon dioxide production. In this study, we investigate the deactivation and reactivation mechanisms of the aqueous Na-CO_2 battery during extended cycling. We have designed the cathode to include non-precious intermetallic catalysts. We have designed the cathode to include non-precious intermetallic catalysts. As the cell undergoes repeated cycles, the voltage polarization during discharge progressively rises, eventually leading to the cell's deactivation and formation of decomposition products clogging the electrode surface. Results obtained from comprehensive characterization techniques, including conductive atomic force microscopy (cAFM), Raman spectroscopy, X-ray photoelectron spectroscopy, X-ray diffraction, and inductively coupled plasma-mass spectrometry provide insight into the decomposition products. We also showcase an electrochemical approach for regeneration of these aqueous cells. Our findings, along with the insights we have gained, provide a path toward creating long-duration systems with self-healing properties.

1. Introduction

The escalating issues of CO_2 emissions, global warming, and the energy crisis represent formidable global challenges. Renewable energy sources stands as the ultimate solution to these pressing challenges, Offering a pathway to significantly reduce CO_2 production, enhance energy security, and lessen dependence on fossil fuels. However, the intermittent nature of renewable energy sources presents a significant hurdle. Thus the development of long-duration energy storage technologies becomes imperative. The ideal solution lies in a technoplogical breakthrough that can effectively decarbonize energy sources while also facilitating long-duration energy storage. Within this framework, metal-CO_2 batteries have garnered substantial interests among scientific communities, policymakers, and funding agencies, owing to their potential in revolutionizing energy storage and utilization. Conventional metal-CO_2 battery efficiently captures CO_2 based on a reversible reaction between CO_2 and M_xCO_3 (M = Na, Li, Mg x = 1 or 2) during the charging-discharging processes [1-10]. Furthermore, the selection of alkali metals plays a critical role in affecting the reaction kinetics, efficiency, processing, fabrication, and overall cost, as each option presents unique advantages and limitations. The selection of the appropriate electrolyte and the strategic design of electrode architecture are crucial factors that significantly influence the electrochemical carbon dioxide reduction process. [11]. Sodium metal batteries hold distinct advantages over other metal-based batteries owing to the abundance of sodium, its cost-effectiveness, and a high theoretical capacity of 1,166 mAh/g. It is noteworthy that Na-ion and Na-air batteries are progressing with the aim to substitute Li-ion batteries in specific applications [12-14]. Moreover, the lower solvation energy of Na-ions in the electrolyte results in reduced charge transfer resistance and enhanced electrode kinetics[15]. However, in conventional metal-CO_2 batteries, the deposition of solid discharge products such as M_2CO_3(s) (M = Li or Na), $Al_2(C_2O_4)_3$(s), or $MgCO_3$(s) onto the electrode surface often leads to clogging of the porous electrode structure. This blockage can result in significant degradation of the electrochemical performance. Initially, it was believed that employing an aqueous system could prevent clogging and the formation of films on the electrode surface. In this context, both the chemical and electrochemical reactions can seamlessly occur during the CO_2 purging and charge/discharge process within the aqueous environment.

In an aqueous CO_2 battery, chemical reactions take place to form carbonic acid followed by the formation of carbonate ions and hydrogen cations according to the following reactions[16-19]:

$$CO_2(aq) + H_2O\ (l) \leftrightarrow H_2CO_3(aq) \qquad (1)$$

$$H_2CO_3(aq) \leftrightarrow HCO_3^-(aq) + H^+(aq) \quad (2)$$

The electrochemical reactions during the discharge proceeds in a double chamber cell where sodium metal is oxidized in the nonaqueous chamber and migrates through the ceramic separator. The following reactions are expected during discharge of the cell [16-18].

$$Na\ (s) \rightarrow Na^+(aq) + e^- \quad (3)$$

$$2H^+(aq) + 2e^- \rightarrow H_2(g) \quad (4)$$

$$HCO^{3-}(aq) + Na^+(aq) \rightarrow NaHCO_3 \quad (5)$$

During the charging process, either oxygen or chlorine evolution reactions are likely to occur, depending on the operational voltage in the double chamber cell configuration [16, 19, 20].

$$2OH^-(aq) \rightarrow O_2(g) + H_2(g) + 2e^- \quad (6)$$

$$2Cl^-(aq) \rightarrow Cl_2(g) + 2e^- \quad (7)$$

$$2Na^+(aq) + 2e^- \rightarrow 2Na\ (s) \quad (8)$$

The electrochemical cell can operate in single or double-chamber configurations depending on the choice of metal electrode and electrolyte solution, as shown in Figures S1a and S1b. In the double-chamber cell configuration, the electrodes are partitioned by an ion-conducting solid electrolyte, such as a NASICON membrane. Within the cathode compartment, the dissolution of CO_2 occurs spontaneously along with the hydrogen evolution reaction on the gas generation electrode side. Depending on the metal anode selected, carbonate by-products are formed. These by-products either accumulate on the electrode or continuously enrich the aqueous medium, thereby maintaining optimal discharge performance, as detailed in the aforementioned reactions [17, 18]. The kinetics of charge-discharge reactions are limited by the ionic conductivity of the solid electrolyte in the dual chamber cell [18]. The electrochemical performance and overall cycling stability of the cell are dictated by the morphology of the electrode and interfacial properties[20-22].

Integrating a non-precious metal oxide or hydroxide catalyst in an aqueous system can remarkably improve the hydrogen evolution reaction within the cathode compartment. On the other hand, the oxygen evolution reaction (OER) typically occurs during water oxidation under both alkaline and acidic conditions, but with sluggish kinetics. Employing seawater as the aqueous medium offers a solution to this challenge by promoting the chlorine evolution reaction while also enabling sodium metal deposition at the anode [23]. Depending on the cell voltage, the system may undergo either a chlorine evolution reaction or an OER. Unlike conventional metal-CO_2 battery systems, the Na-CO2 battery system does not emit CO_2 during charging..

Furthermore, the role of the catalyst in redox reactions and in managing cell voltage polarization is particularly critical from the cost-efficiency perspective.

In this study, we introduced a mixed transition metal hydroxide catalyst and evaluated its electrochemical performance in a Na-CO_2 battery. We used simulated seawater and a nonaqueous medium in a double-chamber cell. During extended discharge cycles in an aqueous medium, we observed the formation of a byproduct on the surface of the cathode catalyst. This byproduct gradually deposits during the discharge, leading to an increase in cell voltage polarization and ultimately causing the deactivation of the cell. Interestingly, we discovered that altering the charging protocol could reactivate the cell and restore its electrochemical performance. To understand the mechanisms behind the deactivation and reactivation, we systematically analyzed four cells at various stages of charge and discharge, the details of which are elucidated in the results and discussion section. Advanced surface characterization techniques, including conductive atomic force microscopy (cAFM)[24], X-ray photoelectron spectroscopy (XPS) along with Raman spectroscopy, scanning electron microscopy (SEM), X-ray diffraction (XRD) and the electrochemical measurements such as electrochemical impedance spectroscopy (EIS), were employed in our study to understand the local electronic conductivity, charge distribution, capacitance development, the interfaces and surfaces properties of electrode and electrolyte in micro- and nanoscale. The results obtained and the fundamental understanding garnered from this analysis are pivotal in constructing a sustainable, long-duration energy storage system in an aqueous medium.

2. Results and Discussion

Figure 1a provides a schematic representation of the operational principle and overall functionality of the aqueous metal-CO_2 cell. Here, CO_2 sourced from an external outlet is purged into the aqueous catholyte solution, which consists of sodium chloride (simulated seawater). The CO_2 undergoes conversion into sodium carbonate, thereby generating energy and evolving hydrogen gas during the discharge process. Unlike conventional metal-CO_2 batteries, the charging process in this system does not involve the decomposition of metal carbonate into regenerated CO_2. Instead, the generation of chlorine or oxygen gas is determined by the operational cell voltage and electrolyte compositions [16, 18, 19]. The electrocatalyst plays a critical role for oxygen evolution reaction (OER). Consequently, a cost-effective, nonprecious bimetallic layered double hydroxide (BLDH) catalyst was synthesized via the co-precipitation method. This catalyst was specifically designed to be compatible with the

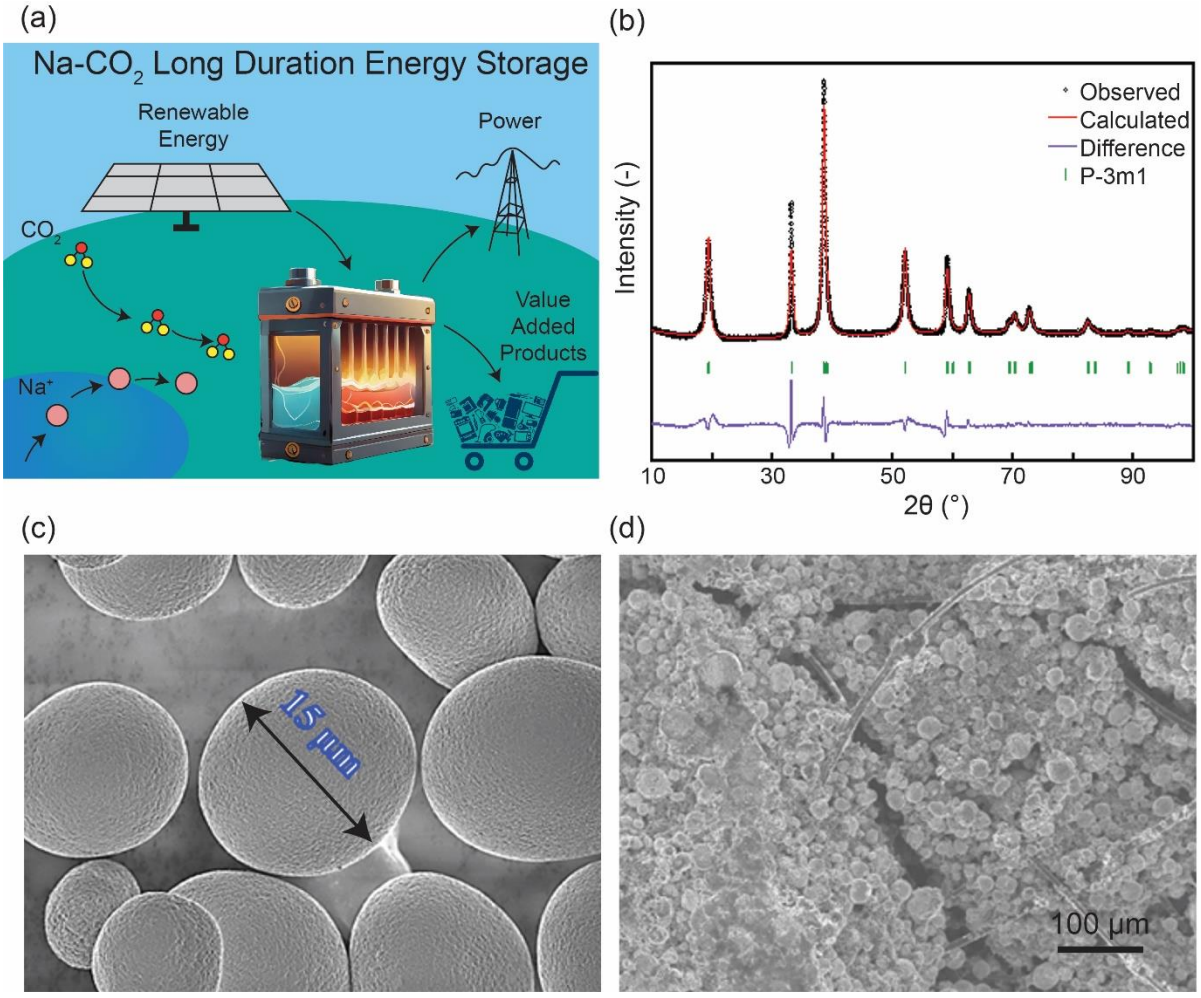

Figure 1: (a) schematic of the operational principle of the aqueous metal-CO_2 battery cell, (b) XRD pattern of the synthesized electrocatalyst, (c) SEM image of the synthesized catalyst and (d) SEM image of fabricated electrode on the carbon cloth.

operating conditions of the aqueous electrolyte. **Figure 1b** and **1c** showcase the X-ray diffraction (XRD) pattern and scanning electron microscopy (SEM) image of the synthesized BLDH, revealing the formation of a pure phase without any impurities. Moreover, the inductively coupled plasma (ICP) analysis confirms the composition, $Ni_{0.89}Fe_{0.11}(OH)_2$, of the synthesized phase. While the SEM image highlights the presence of smooth spherical secondary particles, the relatively larger particle sizes ranging from 10 to 20 µm in diameter results in a comparatively lower surface area. Nonetheless, the catalytic activity of the synthesized BLDH catalyst was evaluated in aqueous system, with the composite electrode being fabricated on a carbon cloth as shown in **Figure 1d**.

Figure 2 is a comparison of the catalytic activity of the commercial Pt/C catalyst in the presence and absence of CO_2. Linear sweep voltammetry (LSV) profiles were measured in seawater at a scan rate of 10 mV/s with Pt/C as the working electrode, Pt as the counter electrode and Ag/AgCl as the reference electrode. The initial pH value for seawater is around 7.33 and the

value for CO_2 saturated seawater is around 4.21. As illustrated in **Figure 2a** and **2b**, the dissolution of CO_2 in seawater fosters an electrochemically advantageous environment that enhances both the hydrogen evolution reaction (HER) and the oxygen evolution reaction (OER) compared to seawater without CO_2 dissolution. A similar trend was observed with the in-house developed catalyst (**Figure S5**).

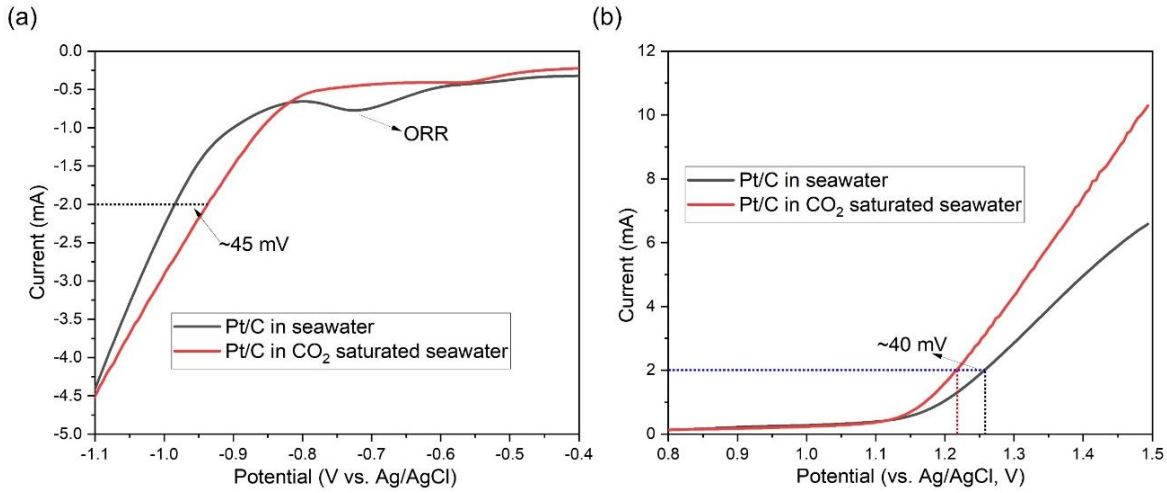

Figure 2: Electrocatalytic activity of commercial Pt/C catalyst in seawater before and after saturation with CO_2. Linear sweep voltammetry (LSV) profiles measured at a scan rate of 10 mV/s for (a) HER and (b) OER activities.

The charge and discharge profiles of the catalyst-coated electrode in CO_2-saturated seawater is displayed in **Figure 3a**, and is compared with the electrode made of baseline empty carbon cloth and commercial Pt/C catalyst, as shown in supplementary **Figure S2**. Notably, the cell voltage polarization during charge-discharge cycles for the electrode with our in-house developed catalyst indicates an enhanced performance compared to the empty carbon cloth. Specifically, the discharge process reached the cut-off voltage promptly (**Figure S2**), demonstrating the remarkable efficiency of the BLDH catalyst in reducing CO_2 within the aqueous system. The operating voltage profile for the commercial Pt/C catalyst ranges between 2 V and 1 V, while the BLDH catalyst cell voltage ranges between 3.5 V and 3.35 V, exceeding that of the commercial Pt/C. **Figure 3a** highlights the smooth charge-discharge cycle of the BLDH catalyst cell over an 80-hour period, exhibiting minimal cell voltage polarization under the applied constant current. However, upon detailed analysis (**Figure 3a**), it becomes evident that there is a gradual increase in the cell polarization during the discharge process, ultimately leading to cell deactivation and an almost complete halt of function during subsequent cycles. Remarkably, in the deactivated state, the cell exhibits a discharge voltage akin to that of the empty carbon cloth electrode (see **Figure 3b** and **S2**). The suspected cause of this decline in

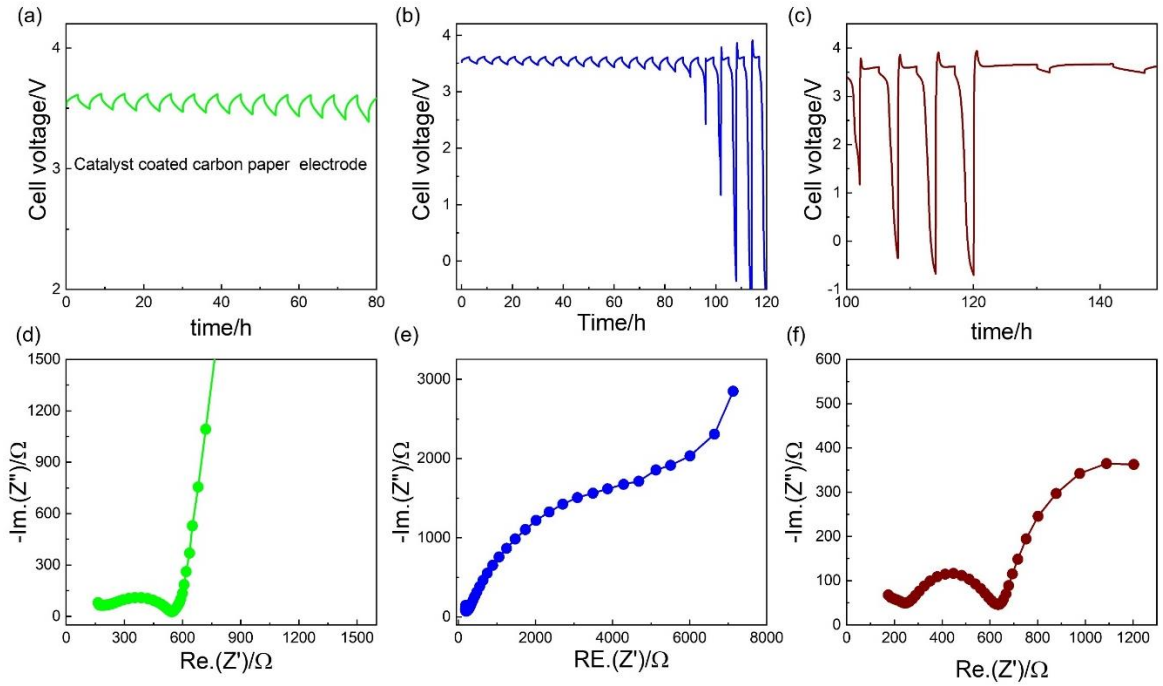

Figure 3: (a) Symmetric charge-discharge profile of catalyst coated carbon cloth electrode, (b) the charge-discharge profile of catalyst coated carbon electrode up to the deactivated state, (c) reactivation of the deactivated cell by a longer time charging the cell from the failure state and impedance measurements of (d) pristine, (e) deactivated, and (f) reactivated cell.

performance is the formation of an insulating surface film on the electrode catalyst, which hinders the redox reaction. It is important to note that the deactivated cell can be reactivated by modifying the charge-discharge protocol, as depicted in **Figure 3c**. Reactivation can be achieved by extended charging of the cell until the insulating layer is removed from the cathode surface (see **Figure 3c**) or by employing an asymmetric charge-discharge cycling protocol, with longer charging periods and shorter discharge times (supplementary **Figure S3a**, 5 hours of charging and 3 hours of discharging). With each asymmetric cycle, there is a noticeable improvement in the discharge cell voltage polarization, accompanied by a decrease in the interfacial charge transfer resistance (**Figure S3a)**. Eventually, the cell fully recovers and functions similarly to a freshly assembled cell. The key advantage of the asymmetric charge-discharge cycling protocol is that it allows the cell to remain operational while recovering from the failure state. Electrochemical impedance spectroscopy was utilized to analyze the cell at three distinct stages: before cycling, during deactivation, and post-recovery from deactivation, as depicted in **Figures 3d, e,** and **f**. This analysis revealed that both the pristine and the recovered cell exhibit similar levels of bulk and interfacial resistances, which are significantly lower than those observed in the deactivated cell. Notably, the interfacial resistance of the deactivated cell is significantly higher than in the pristine and recovered cell, exceeding by more than an order of magnitude. These findings strongly suggest the formation of an insulating

protective layer on the catalyst surface of the cathode during prolonged cycling. The composition of this insulating layer is hypothesized to predominantly consist of sodium-based products, considering the absence of other metallic element in the solution. Initially, it was anticipated that the sodium-based products would either dissolve in the solution or precipitate within the container, rather than accumulating on the cathode surface. However, the results obtained indicate that a fraction of the sodium-based product gradually deposits on the surface throughout the cycling process, while the remaining portion enriches the solution.

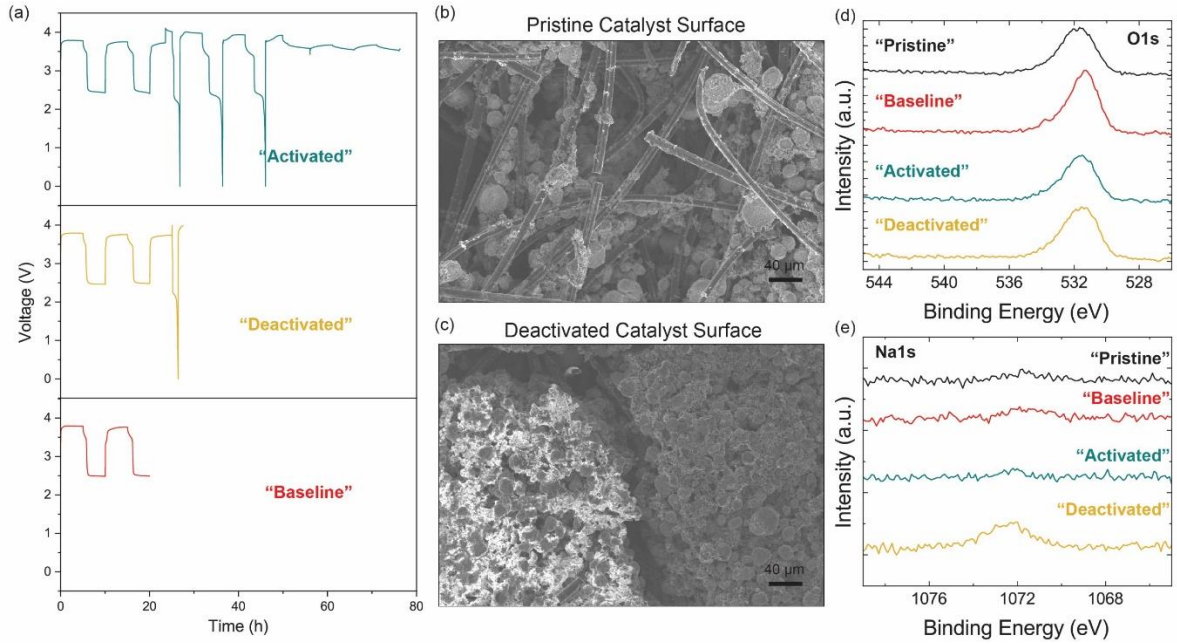

Figure 4: (a) assembling three cells to deliberately deactivated, reactivated and forming a baseline cell, (b) SEM micrographs of deactivated and reactivated catalyst coated electrodes, (c) XPS spectra of O1s and Na1s of pristine, baseline, reactivated and deactivated electrodes.

To gain a deeper understanding of the deposited products on the electrode surface, three separate cells were assembled and subjectrred to deliverate deactivation, reactivation, and preservation after a few cycles, as depicted in **Figure 4a**. These cells were then compared with the pristine cell. The SEM image of the deactivated cell clearly shows the presence of a bright layer covering the electrode surface. Upon reactivation, achieved through an extended charging process, it was observed that most of the deposited film had been removed from the electrode surface (**Figure 4b**). This finding underscores the dynamic reversibility of the film, highlighting its susceptibility to electrochemical oxidation and subsequent disintegration. XPS analysis revealed that there were no noticeable changes occurred in the O1s spectrum across all four sample as seen in **Figure 4c**. However, an intriguing effect is observed in the Na 1s spectrum. Specifically, a distinct peak at around 1072 eV was identified in the deactivated electrode, whereas this peak was absent in the spectra of the other electrodes. These findings suggest that

the Na 1s peak observed in the CO_2 reduction product may correspond to the presence of sodium oxalate ($Na_2C_2O_4$) or hydrogen bicarbonate ($NaHCO_3$), both of which have a binding energy of around 1072 eV [25].

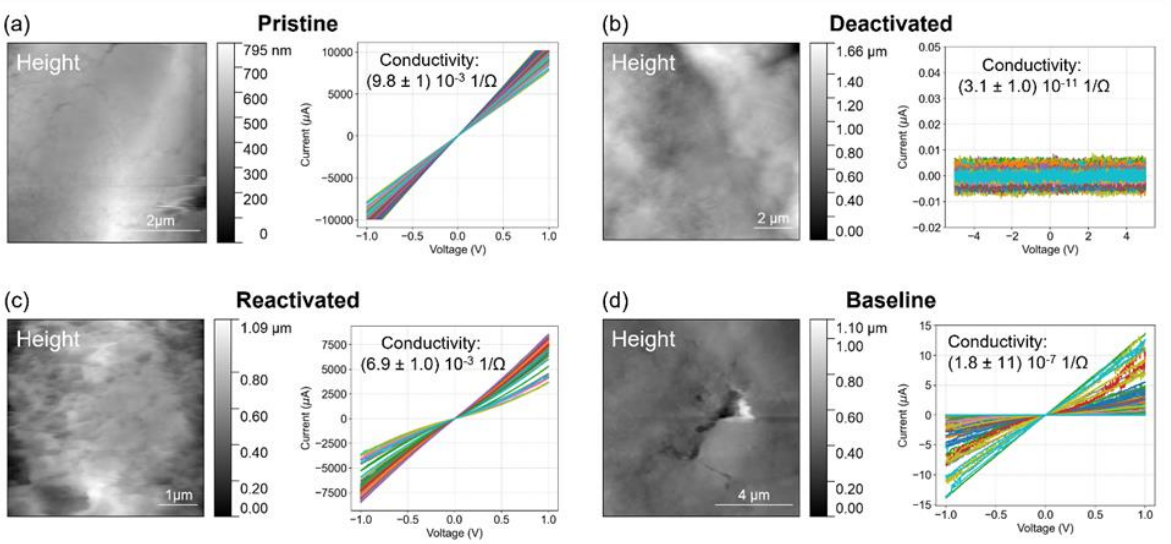

Figure 5: AFM height maps showing the morphology (left) and I-V curves for (a) pristine, (b) deactivated, (c) reactivated and (d) baseline cells. The I-V graphs show the curves plotted for all pixels. The conductivity was obtained from the slope of all shown I-V curves and subsequently calculating the mean and standard deviation values for the entire grid. Note that standard deviation in (d) is so large because most pixels of this grid did not show any conductivity (see maps in Figure S4).

The cAFM measurements were performed on pristine, baseline, deactivated, and reactivated samples for electrode morphology, surface current distribution and electronic conductivity. **Figure 5** shows the morphology and the conductivity of the samples measured with cAFM. The spatial distribution of the conductivity is shown in supplementary **Figure S4**. The pristine cell shows the smoothest surface and highest conductivity (**Figure 5a**). No current could be detected on the deposits film of the deactivated cell and the surface morphology is much rougher (**Figure 5b**) than the pristine cell. The reactivated cell showed conductive areas, however, some I-V curves exhibit nonlinear contributions to the overall current (**Figure 5c**). On the baseline cell, some pixels with high conductivity were detected (**Figure 5d**). However, due to the presence of many non-conductive pixels (see conductivity maps in **Figure S4**), the standard deviation of the mean conductivity is very high. Deactivation of the electrode is originated due to the formation of electronically insulating surface film which prevents the further redox reaction at catalyst surface.

In spite of differences in electronic conductivity and surface current distribution (**Figure S4**) of the four different samples only the deactivated sample exhibits presence of x-ray peak for surface film at around 43-degree two theta value and no effect was appeared for other three

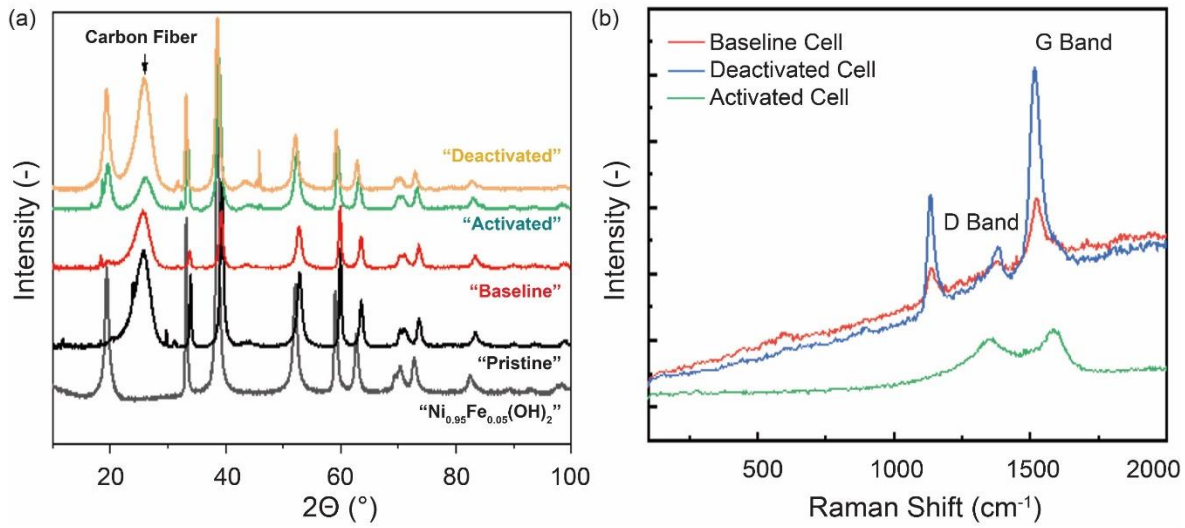

Figure 6: (a) X-ray diffraction patterns and (b) Raman spectra of pristine, baseline, reactivated and deactivated cells obtained from the electrochemical measurements.

samples at the same position (**Figure 6a**). On the other hand, the deactivated and baseline samples show only the Raman peak shift at 1140 cm^{-1} and other two samples do not show any shift at the same position. The peaks centered at 1384 cm^{-1} and 1600 cm^{-1} are ascribed to the carbon D-band and G-band, respectively [26]. As can be seen from **Figure 6b**, all three samples feature the D and G bands, representing the carbon current collector. However, only the baseline and deactivated cells exhibit the CO_2 reduction product, sodium oxalate at 1140 cm^{-1} [27]. The deactivated cells present a noticeably higher concentration of oxalate products due to the gradually accumulation of the oxalate products on the electrode surface till completely deactivation of the cell. From the characterization techniques, it can be inferred that sodium oxalate is the most likely composition of the insulating surface film.

3. Conclusion

In this work, a cost-effective, bimetallic catalyst comprising Ni and Fe has been synthesized, upscaled, and optimized in terms of composition and morphology. This catalyst significantly reduces the charge-discharge cell voltage polarization, outperforming both the standard carbon paper electrode and the commercial Pt/C catalyst electrode at equivalent current rates. Despite its effectiveness, the catalyst-electrode experiences deactivation after approximately 100 hours of operation. However, modifying the charge-discharge protocol has proven successful in reactivating the cell. Postmortem analysis unveiled the gradual buildup of an insulating sodium oxalate layer on the catalyst electrode surface during symmetric charge-discharge cycles. By applying either a prolonged charging approach or an asymmetric cycling approach, the cell was effectively revived from its failure state. These operational advancements have paved the way for a potentially sustainable, long-duration energy storage system.

4. Experimental Section/Methods

4.1. Synthesis of Materials

The Ni1-xFex$(OH)_2$ electrocatalyst was synthesized by coprecipitation process using $NiSO_4 \cdot 6H_2O$ (Aldrich) and $FeSO_4 \cdot 7H_2O$ (Aldrich) as the precursors. A detailed synthesis procedure can be found in our previous report [25]. In short, the solutions were used in the coprecipitation process denoted as solutions A, B, and C. Solution A consisted of pure deionized water which was first added to the reactor vessel and was then maintained at 55 °C at 500 rpm. Solution B comprised of $NiSO_4 \cdot 6H_2O$ (Aldrich) and $FeSO_4 \cdot 7H_2O$ (Aldrich) at appropriate Ni and Fe ratios dissolved in deionized water at a concentration of 2M. Solution C was made by mixing NaOH (Aldrich) and NH4OH (Aldrich) at 2M concentration in deionized water. Solution C was first added to solution A in the CSTR at a flow rate of 1lml/h to raise the pH of the reactor contents from near neutral to ~11.5. After reaching the constant pH value of ~11.5, solution B was added to the CSTR at a flow rate of 750ml/h continuously. The pH was maintained in the limits of 11.45-11.55 by adding the solution C to the reactor if the pH fell below 11.45. The $Ni_{1-x}Fe_x(OH)_2$ precipitation was collected as a continuous stream through the exit port of the reactor and particle morphology was checked unit morphological uniformity was observed. The resulting $Ni_{1-x}Fe_x(OH)_2$ precipitation was then filtered and washed with deionized water several times until the pH of the filtrate pH was close to 7.0 with the removal of sulfate content. The filtrate was then dried at 120 °C overnight in a vacuum oven and was then ground using mortar and pestle.

4.2. Characterization

To assess the purity of the synthesized $Ni_{1-x}Fe_x(OH)_2$ sample, X-ray Diffraction (XRD) measurements were performed. The data was collected at room temperature over the 2θ angular range of $10° \leq 2\theta \leq 100°$ with a step size of 0.01° using a Bruker D8 ADVANCE diffractometer operating with Cu-Kα radiation. The morphology of the $Ni_{1-x}Fe_x(OH)_2$ materials and the fabricated electrode before and after electrochemical cycling were characterized using scanning electron microscopy (SEM) with energy dispersive X-ray (EDX) elemental analysis on a ThermoFisher Scientific Scios 2 Dual Beam Focused Ion Beam/scanning electron microscope. The composition of the synthesized powders was determined by Inductively Coupled Plasma Optical Emission Spectrometer (ICP-OES, Agilent Technologies 5110). The samples were dissolved in an HF solution and then diluted in 2 wt.% HNO_3 for ICP measurement. The Raman mapping was collected on a confocal Raman spectrometer (Horiba, 405 nm edge, objective = 50×, a grating with 2400 grooves/ mm, numerical aperture (N.A.) = 0.42, local power <500

μW). The laser spot diameter was estimated to be 1 μm. The scan region was set to be 50 μm x 50 μm, with the step size of 1×1 μm^2/pixel. The integration time was set to 3 s for each point. Autofocus mode was applied at each step to assure consistent focus on the sample surface. All Raman mappings were analyzed using Horiba Labspec 6 imaging and spectroscopy software and the K-means clustering algorithm integrated into the Scikit-learn platform with a previously reported similar method [26, 27].

4.3. Electrode Fabrication

90% synthesized electrocatalyst, $Ni_{1-x}Fe_x(OH)_2$, was mixed with 5% carbon black and 5% PVDF binder in an ethanol solvent to make a homogeneous slurry with optimum viscosity. The resulting slurry was cast on the carbon cloth (MSE materials) current collector by doctor's blade processing and the casted film was dried overnight in the vacuum oven at 120 °C. The dried film was punched into a spherical electrode with a diameter of 12mm. Alternatively, catalyst ink was prepared by mixing with 5% carbon black and 5% PVDF binder in NMP solvent. The resulting ink was dropped onto the activated carbon cloth by pipette in order to load the catalyst not only on the surface of the carbon paper but also into the interior pores.

4.4. Electrochemical Measurements

The schematic of the metal-CO2 battery cell is displayed in supplementary Figures S1a and S1b. The catalyst-coated cathode emerged in a simulated aqueous seawater catholyte containing 200ml of electrolyte solution and metallic sodium was kept in a nonaqueous solution and hermetically sealed in a coin cell configuration as shown in Figure S1b. In the double chamber, the aqueous catholyte and nonaqueous anolyte were separated by sodium ion conducting solid-state electrolyte (NASICON). The CO2 gas was purged into the catholyte chamber. Galvanostatic charge/discharge tests were performed on Bio-Logic battery testing systems under various current densities. The electrochemical impedance spectroscopy (EIS) measurements were performed to determine the interfacial charge transfer resistance at different states of cycling the cell. Before EIS measurements the cell voltage was relaxed to a steady state condition and measurement was performed in the frequency range of 5 MHz to 0.5 Hz using a sinusoidal voltage amplitude of 10 mV. The measured EIS spectra were fitted using an equivalent circuit model.

4.5. Conductive Atomic Force Microscopy Measurements

The nanoscale cAFM measurements were performed using an Asylum Research Cypher atomic force microscope equipped with conductive Nanosensor PPP-EFM tips (nominal force constant 2.8 N/m, nominal resonant frequency 75 kHz). As shown in the schematic depiction in supplementary Figure S1c, the tip was connected to a voltage source provided by the atomic

force microscope controller. To measure the current, a FEMTO DLPCA-200 current amplifier was used. The shown cAFM data was acquired in spectroscopy mode where the tip is placed at each pixel within a specified grid and a voltage is applied to the tip while simultaneously measuring the current, resulting in current-voltage (I-V) curves. The voltage waveform is triangular with an amplitude of 1 V (pristine, reactivated, baseline) or 5 V (deactivated) and a frequency of 1 Hz. Conductivity values were obtained by linear fitting of the I-V curves and extracting the slope. The conductivity values stated here are mean and standard deviation averaged over the whole grid of the shown area. The height maps showing the surface morphology were acquired in contact mode in which the tip scans the sample surface upon maintaining a constant contact force that is inferred from the deflection of the cantilever that the tip is mounted on and measured using a position sensitive photodetector. Several maps were acquired for each cell status and each sample had some areas that were not conductive within the scope of these measurements, which is likely due to local interruptions in the conductive path.

Supporting Information

Supporting Information is available from the Wiley Online Library or from the author.

Acknowledgements

This research at Oak Ridge National Laboratory, managed by UT Battelle, LLC, for the U.S. Department of Energy (DOE) under contract DE-AC05-00OR22725, was sponsored by Laboratory Directed Research and Development (LDRD) Program at Oak Ridge National Laboratory with project number 11060. The conductive atomic force microscopy experiments were supported by the Center for Nanophase Materials Sciences (CNMS), which is a US Department of Energy, Office of Science User Facility at Oak Ridge National Laboratory.

Received: ((will be filled in by the editorial staff))

Revised: ((will be filled in by the editorial staff))

Published online: ((will be filled in by the editorial staff))

References

[1] Y. Xing, K. Wang, N. Li, D. Su, W.-T. Wong, B. Huang, S. Guo, Ultrathin RuRh Alloy Nanosheets Enable High-Performance Lithium-CO2 Battery, Matter, 2 (2020) 1494-1508.
[2] Y. Qiao, Y. Liu, C. Chen, H. Xie, Y. Yao, S. He, W. Ping, B. Liu, L. Hu, 3D-Printed Graphene Oxide Framework with Thermal Shock Synthesized Nanoparticles for Li-CO2 Batteries, Advanced Functional Materials, 28 (2018) 1805899.

[3] W. Ma, S. Lu, X. Lei, X. Liu, Y. Ding, Porous Mn2O3 cathode for highly durable Li–CO2 batteries, J. Mater. Chem. A, 6 (2018) 20829-20835.
[4] W. Ma, X. Liu, C. Li, H. Yin, W. Xi, R. Liu, G. He, X. Zhao, J. Luo, Y. Ding, Rechargeable Al–CO2 Batteries for Reversible Utilization of CO2, Advanced Materials, 30 (2018) 1801152.
[5] B. Liu, Y. Sun, L. Liu, J. Chen, B. Yang, S. Xu, X. Yan, Recent advances in understanding Li–CO2 electrochemistry, Energy Environ. Sci., 12 (2019) 887-922.
[6] Y. Li, J. Zhou, T. Zhang, T. Wang, X. Li, Y. Jia, J. Cheng, Q. Guan, E. Liu, H. Peng, B. Wang, Highly Surface-Wrinkled and N-Doped CNTs Anchored on Metal Wire: A Novel Fiber-Shaped Cathode toward High-Performance Flexible Li–CO2 Batteries, Advanced Functional Materials, 29 (2019) 1808117.
[7] S. Li, Y. Dong, J. Zhou, Y. Liu, J. Wang, X. Gao, Y. Han, P. Qi, B. Wang, Carbon dioxide in the cage: manganese metal–organic frameworks for high performance CO2 electrodes in Li–CO2 batteries, Energy Environ. Sci., 11 (2018) 1318-1325.
[8] C. Li, Z. Guo, B. Yang, Y. Liu, Y. Wang, Y. Xia, A Rechargeable Li-CO2 Battery with a Gel Polymer Electrolyte, Angewandte Chemie International Edition, 56 (2017) 9126-9130.
[9] F. Cai, Z. Hu, S.-L. Chou, Progress and Future Perspectives on Li(Na)–CO2 Batteries, Advanced Sustainable Systems, 2 (2018) 1800060.
[10] W.I. Al Sadat, L.A. Archer, The O2-assisted Al/CO2 electrochemical cell: A system for CO2 capture/conversion and electric power generation, Science Advances, 2 e1600968.
[11] A. Jena, Z. Tong, H. Chang, S.-F. Hu, R.-S. Liu, Capturing carbon dioxide in Na–CO2 batteries: A route for green energy, Journal of the Chinese Chemical Society, 68 (2021) 421-428.
[12] C. Vaalma, D. Buchholz, M. Weil, S. Passerini, A cost and resource analysis of sodium-ion batteries, Nature Reviews Materials, 3 (2018) 18013.
[13] P.K. Nayak, L. Yang, W. Brehm, P. Adelhelm, From Lithium-Ion to Sodium-Ion Batteries: Advantages, Challenges, and Surprises, Angewandte Chemie International Edition, 57 (2018) 102-120.
[14] I. Hasa, S. Mariyappan, D. Saurel, P. Adelhelm, A.Y. Koposov, C. Masquelier, L. Croguennec, M. Casas-Cabanas, Challenges of today for Na-based batteries of the future: From materials to cell metrics, Journal of Power Sources, 482 (2021) 228872.
[15] M. Okoshi, Y. Yamada, A. Yamada, H. Nakai, Theoretical Analysis on De-Solvation of Lithium, Sodium, and Magnesium Cations to Organic Electrolyte Solvents, Journal of The Electrochemical Society, 160 (2013) A2160.
[16] J. Xie, Z. Zhou, Y. Wang, Metal–CO2 batteries at the crossroad to practical energy storage and CO2 recycle, Advanced Functional Materials, 30 (2020) 1908285.
[17] J. Kim, A. Seong, Y. Yang, S. Joo, C. Kim, D.H. Jeon, L. Dai, G. Kim, Indirect surpassing CO2 utilization in membrane-free CO2 battery, Nano Energy, 82 (2021) 105741.
[18] C. Kim, J. Kim, S. Joo, Y. Yang, J. Shin, M. Liu, J. Cho, G. Kim, Highly Efficient CO2 Utilization via Aqueous Zinc– or Aluminum–CO2 Systems for Hydrogen Gas Evolution and Electricity Production, Angewandte Chemie International Edition, 58 (2019) 9506-9511.
[19] C. Kim, J. Kim, S. Joo, Y. Bu, M. Liu, J. Cho, G. Kim, Efficient CO2 Utilization via a Hybrid Na-CO2 System Based on CO2 Dissolution, iScience, 9 (2018) 278-285.
[20] A. Wang, X. Hu, H. Tang, C. Zhang, S. Liu, Y.-W. Yang, Q.-H. Yang, J. Luo, Processable and Moldable Sodium-Metal Anodes, Angewandte Chemie International Edition, 56 (2017) 11921-11926.
[21] Y. Zhao, L.V. Goncharova, A. Lushington, Q. Sun, H. Yadegari, B. Wang, W. Xiao, R. Li, X. Sun, Superior Stable and Long Life Sodium Metal Anodes Achieved by Atomic Layer Deposition, Advanced Materials, 29 (2017) 1606663.

[22] H. Wang, C. Wang, E. Matios, W. Li, Critical Role of Ultrathin Graphene Films with Tunable Thickness in Enabling Highly Stable Sodium Metal Anodes, Nano Letters, 17 (2017) 6808-6815.
[23] S.M. Hwang, J.-S. Park, Y. Kim, W. Go, J. Han, Y. Kim, Y. Kim, Rechargeable Seawater Batteries—From Concept to Applications, Advanced Materials, 31 (2019) 1804936.
[24] C. Rodenbücher, M. Wojtyniak, K. Szot, Conductive AFM for Nanoscale Analysis of High-k Dielectric Metal Oxides, in: U. Celano (Ed.) Electrical Atomic Force Microscopy for Nanoelectronics, Springer International Publishing, Cham, 2019, pp. 29-70.
[25] S. Ivanova, E. Zhecheva, R. Kukeva, D. Nihtianova, L. Mihaylov, G. Atanasova, R. Stoyanova, Layered P3-NaxCo1/3Ni1/3Mn1/3O2 versus Spinel Li4Ti5O12 as a Positive and a Negative Electrode in a Full Sodium–Lithium Cell, ACS Appl. Mater. Interfaces, 8 (2016) 17321-17333.
[26] J.A. Smith, O.S. Game, J.E. Bishop, E.L.K. Spooner, R.C. Kilbride, C. Greenland, R. Jayaprakash, T.I. Alanazi, E.J. Cassella, A. Tejada, G. Chistiakova, M. Wong-Stringer, T.J. Routledge, A.J. Parnell, D.B. Hammond, D.G. Lidzey, Rapid Scalable Processing of Tin Oxide Transport Layers for Perovskite Solar Cells, ACS Applied Energy Materials, 3 (2020) 5552-5562.
[27] B.K.S. Pandey, A.; Sinha, A. K.; Gopal, R., Synthesis and Characterization of Cobalt Oxalate Nanomaterial for Li-Ion Battery, Materials Focus, 4 (2015) 333-337.